JOURNAL OF COMPUTATIONAL PHYSICS 107, 10-22 (1993)

Non-oscillatory Spectral Element Chebyshev Method for Shock Wave Calculations

DAVID SIDILKOVER AND GEORGE EM KARNIADAKIS

Department of Mechanical and Aerospace Engineering, Program in Applied and Computational Mathematics, Princeton University, Princeton, New Jersey 08544

Received July 29, 1991; revised July 16, 1992

A new algorithm based on spectral element discretization and non-oscillatory ideas is developed for the solution of hyperbolic partial differential equations. A conservative formulation is proposed based on cell averaging and reconstruction procedures, that employs a staggered grid of Gauss-Chebyshev and Gauss-Lobatto Chebyshev discretizations. The non-oscillatory reconstruction procedure is based on ideas similar to those proposed by Cai *et al.* (*Math. Comput.* **52**, 389 (1989)) but employs a modified technique which is more robust and simpler in terms of determining the location and strength of a discontinuity. It is demonstrated through model problems of linear advection, inviscid Burgers equation, and one-dimensional Euler system that the proposed algorithm leads to stable, non-oscillatory accurate results. Exponential accuracy away from the discontinuity is realized for the inviscid Burgers equation example.

1. INTRODUCTION

Spectral element methods are high-order weighted residual techniques for the solution of partial differential equations typically encountered in fluid dynamics [14, 12]. Their success in the recent past in simulating complex flows derives from the flexibility of the method in representing accurately non-trivial geometries while preserving the good resolution properties of spectral methods [11]. In these simulations, however, both the geometry and the solution are described through smooth functions so that spectral element methods can obtain exponential accuracy by fully exploiting that regularity. There are numerous fluid dynamics applications, however, where either very steep gradients or even jump-discontinuities are present, e.g., interfaces in multiphase flows, flame fronts, or shocks in compressible flows. A straightforward application of high-order numerical methods in these situations is not possible, as large errors induced by the discontinuity (Gibbs phenomenon) propagate in the domain and eventually render the solution with oscillations everywhere.

One approach to successfully simulating the aforementioned complex flows is to use essentially non-oscillatory pseudospectral schemes developed for systems of hyperbolic partial differential equations

$$\mathbf{u}_t + \mathbf{f}(\mathbf{u})_x = 0 \tag{1}$$

(see [2] for the case of Fourier method). The main idea is to augment the spectral space by adding a non-smooth function, representing discontinuity. A conservative scheme can be obtained by defining cell averaged quantities in following the work of Cai *et al.* for Chebyshev methods [1]. A staggered grid of Gauss–Chebyshev and Gauss–Chebyshev–Lobatto collocation points is employed to accomodate the cell averages and point values. Point values are obtained from cell averages by using appropriate reconstruction procedure (possibly essentially non-oscillatory).

Although very accurate, the non-oscillatory spectral methods described in these previous works are limited to computational domains with highly regular nodal point distribution and periodic boundary conditions as in Fourier method or more general boundary conditions but on a single domain. In the current work we attempt to relax these constraints by substituting for the higher-order scheme a spectral element discretization method [14, 12]. In the spectral element discretization the computational domain is broken up into several subdomains (macro-elements) within which data and unknowns are represented as spectral expansions in terms of general eigenfunctions—solutions of the singular Sturm–Liuville problems, i.e., Chebyshev polynomials, Legendre polynomials, etc. The discrete equations are derived via variational statements, so that the unknowns at each node represent values of the unknown field variable. This approach and its variants [11, 16, 13] results in exponential (spectral-like) convergence for infinitely smooth solutions.

The main idea presented in this work is to modify the Chebyshev Lagrangian interpolant basis of the spectral

0021-9991/93 $5.00

element formulation by adding a non-smooth function, representing discontinuity. A new robust and efficient technique is also proposed for estimating the discontinuity location and strength. As a result the proposed non-oscillatory reconstruction procedure implemented on a staggered Chebyshev spectral element grid leads to stable solutions free of oscillations. The incorporation of a high-order filter [20] results in recovering high-order accuracy away from discontinuity.

The paper is organized as follows: In Section 2, we introduce the basic ideas upon which our conservative spectral element formulation is based (cell averaging and reconstruction procedures). In Section 3, the non-oscillatory cell averaging and reconstruction are presented. In Section 4, we describe the model problems used in this work along with some additional aspects of reconstruction (interfacial constraint). In Section 5, we describe the algorithm and briefly review its components (time-marching scheme, filter, flux limiter). Finally, results are presented in Section 6, followed by a brief discussion in Section 7.

2. CELL AVERAGES AND RECONSTRUCTION: SMOOTH FUNCTION

2.1. *Cell Averages*

In the general case that we consider in this work the nodal points are distributed in a non-uniform manner and thus we need to define appropriate cell averaged quantities. In particular, adopting the terminology explained in Fig. 1 the cell averaged velocity $\bar{u}_j$ is given by

$$\bar{u}_j \equiv \bar{u}(x_j, t) = \frac{1}{x_{i^+} - x_{i^-}} \int_{x_{i^-}}^{x_{i^+}} u(x, t)\, dx. \tag{2}$$

Given this definition, Eq. (1) can be integrated along a cell extending from i^- to i^+ as

$$\frac{d\bar{u}_j}{dt} + \frac{f(u_{i^+}) - f(u_{i^-})}{\Delta x_j} = 0, \tag{3}$$

where we have also defined

$$\Delta x_j \equiv x_{i^+} - x_{i^-}. \tag{4}$$

The above equation therefore suggests that the fluxes $f(u)$ should be evaluated at the ends of the cell using *de-averaged* (reconstructed) velocity values; this formulation leads to the conservative (or flux) form of the semi-discrete wave equation. In the following, we define cell averaged quantities for two particular discretizations: first, spectral (Chebyshev) discretizations; and second, spectral element (Chebyshev) discretizations. Proceeding with the first case we refer to Fig. 1, where the set of points j denote the cell at which cell averaged quantities are defined.

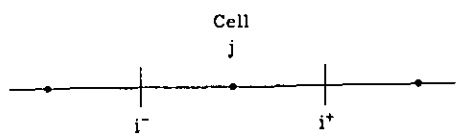

FIG. 1. Cell averaged quantities are defined at the Gauss points j and point values are defined at the Gauss–Lobatto points i.

A spectral-Chebyshev expansion corresponds to a non-uniform distribution of points with cells of variable size Δx_j. Following the formulation of Cai *et al.* [1] we select the set of points j to be the Gauss–Chebyshev points (see Fig. 2) defined by

$$x_j = -\cos((j - 1/2)\,\Delta\theta), \quad \text{where} \quad \Delta\theta = \pi/N, \quad 1 \leqslant j \leqslant N, \tag{5}$$

and the end points i^+, i^- of each cell are the Gauss–Lobatto points defined as

$$x_i = -\cos(i\,\Delta\theta), \qquad 0 \leqslant i \leqslant N. \tag{6}$$

Using these two sets of points and the definition (2), a Chebyshev spectral expansion then of the form

$$u(x) = \sum_{k=0}^{N} a_k T_k(x), \tag{7}$$

after averaging becomes

$$\bar{u}(x) = \sum_{k=0}^{N} a_k \bar{T}_k(x), \tag{8}$$

where the cell averaged Chebyshev polynomial is given by

$$\bar{T}_0 = 1 \tag{9a}$$

$$\bar{T}_1 = \tfrac{1}{2}\sigma_1 U_1(x) \tag{9b}$$

$$\bar{T}_k = \tfrac{1}{2}[\sigma_k U_k(x) - \sigma_{k-2} U_{k-2}(x)] \qquad \forall k \geqslant 2, \tag{9c}$$

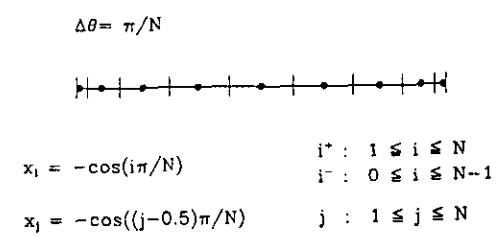

FIG. 2. Spectral Chebyshev method. The set of points j defines the cell averaged quantities, while the point values i are used in evaluating the fluxes.

where

$$\sigma_k = \frac{\sin(k+1)(\Delta\theta/2)}{(k+1)\sin(\Delta\theta/2)}. \tag{10}$$

Here we have introduced $U_k(x) = (1/(k+1))\, T'_{k+1}(x)$ to be the second kind of the Chebyshev polynomials.

In the spectral element discretization the domain is broken up into several macro-elements (Fig. 3) within which the velocity is expanded in terms of Chebyshev polynomials. Here, we establish the connection between the local (elemental) reference system and the global (physical) coordinate system. For the set of Gauss–Lobatto–Chebyshev points their local coordinate in the kth element is given by

$$r_i^k = -\cos\left(\frac{\pi i}{N}\right), \qquad 0 \leqslant i \leqslant N \tag{11}$$

which are related to the global coordinate x through the equation

$$x = \frac{L_k}{2} r^k + \frac{x_L^k + x_R^k}{2}; \tag{12}$$

here x_L^k and x_R^k denote the left and right coordinates of the elemental boundaries, and L_k is the element length.

The interpolant of $u(x)$ in the kth element is then represented as

$$u^k(r) = \sum_{i=0}^{N} h_i(r^k)\, u_i^k. \tag{13}$$

Here, u_i^k are nodal values of u, and h_i are shape functions corresponding to element k and node i, with property $h_i(r_j^k) = \delta_{ij}$, (where δ_{ij} is the Kronecker-delta symbol). Expressions for these Lagrangian interpolants (as well as for their derivatives) in terms of Chebyshev or Legendre polynomials can be found in [9]. In the kth element an expansion of the form

$$u^k(x) = \sum_{i=0}^{N} u_i^k h_i(x) \tag{14}$$

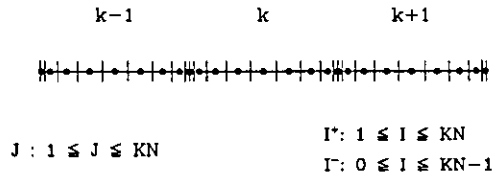

FIG. 3. Spectral element Chebyshev discretization. J's are used for global indexing of cell averaged quantities and I's, for global indexing of point values.

defined on the Gauss–Lobatto–Chebyshev points after the application of the averaging operator takes the form

$$\bar{u}^k(x) = \sum_{i=0}^{N} u_i^k \bar{h}_i(x), \tag{15}$$

where u_i^k are the point values for element k and x refers to the local coordinate; $h_i(x)$ and $\bar{h}_i(x)$ are the Gauss–Lobatto–Chebyshev–Lagrangian interpolant and its corresponding cell averaged function obtained from

$$h_i(x) = \frac{2}{N} \sum_{p=0}^{N} \frac{1}{\bar{c}_i \bar{c}_p} T_p(x_i)\, T_p(x), \qquad 0 \leqslant i \leqslant N \tag{16}$$

$$\bar{h}_i(x) = \frac{2}{N} \sum_{p=0}^{N} \frac{1}{\bar{c}_i \bar{c}_p} T_p(x_i)\, \bar{T}_p(x), \qquad 0 \leqslant i \leqslant N, \tag{17}$$

where $c_n = 1$ if $n \neq 0, N$ and $c_n = 2$ otherwise. In matrix form the above cell averaging procedure can be written as

$$\bar{u}_j^k = \mathbf{A}_{ji}^k \mathbf{u}_i^k, \qquad 0 \leqslant i \leqslant N, \quad 0 \leqslant j \leqslant N, \tag{18}$$

where the cell averaging matrix is defined as $A_{ji}^k = \bar{h}_i(x_j)$; here x_j refers to a local coordinate. Based on the nodal cell averaged values obtained from (18) the corresponding polynomial can be constructed using Lagrangian interpolation; i.e.,

$$\bar{u}(x) = \sum_{j=1}^{N} \bar{u}_j^k\, g_j(x), \tag{19}$$

where the Gauss–Chebyshev–Lagrangian interpolant is given by

$$g_j(x) = (-1)^{j+1} \frac{1 - x_j^2}{x - x_j} \frac{T_N(x)}{N}, \qquad 1 \leqslant j \leqslant N. \tag{20}$$

Having constructed a cell averaging procedure for the spectral element discretization we proceed next with the inverse operation of de-averaging and recovering point values for the evaluation of fluxes in Eq. (3).

2.2. *Reconstruction and Point Values*

The reconstruction operation can also be put into matrix form. We consider first the polynomial describing the cell averaged values,

$$\bar{u}(x) = \sum_{j=1}^{N} \bar{u}_j^k\, g_j(x). \tag{21}$$

An alternative to expression to (20) for the Gauss–Chebyshev–Lagrangian interpolant is

$$g_j(x) = \sum_{p=0}^{N-1} \frac{2}{N\bar{c}_p} T_p(x_j)\, T_p(x). \tag{22}$$

We can also express the $g_j(x)$ in terms of the second kind Chebyshev polynomials; to this end we recall that

$$T_p(x) = \tfrac{1}{2}[U_p(x) - U_{p-2}(x)], \qquad \forall p \geqslant 2. \tag{23}$$

Using the above equation we can rewrite $g_j(x)$ as

$$g_j(x) = \sum_{p=0}^{N-1} \lambda_p^j U_p(x), \qquad 1 \leqslant j \leqslant N. \tag{24}$$

Here we have defined

$$\lambda_p^j = \frac{1}{N} T_p(x_j) \qquad \text{for} \quad p = N-2, N-1 \tag{25a}$$

$$\lambda_p^j = \frac{1}{N}[T_p(x_j) - T_{p+2}(x_j)] \qquad \text{for} \quad 0 \leqslant p \leqslant N-3. \tag{25b}$$

The interpolating polynomial corresponding to point values (Gauss–Chebyshev–Lobatto points) can then constructed using the *de-averaged* Lagrangian interpolants G_j as

$$u(x) = \sum_{j=1}^{N} \bar{u}_j^k G_j(x). \tag{26}$$

The cell averaged second kind Chebyshev polynomial is obtained using the definition of Eq. (2) (see details in [1]),

$$\bar{U}_p(x) = \sigma_p U_p(x) \tag{27}$$

with σ_p obtained from Eq. (10). To determine $G_j(x)$ therefore we consider (26)–(27) and (21)–(24) and thus we obtain

$$G_j(x) = \sum_{p=0}^{N-1} \frac{\lambda_p^j}{\sigma_p} U_p(x). \tag{28}$$

To recover the point values u_i we simply set $x = x_i$ in the interpolating polynomial $u(x)$. In matrix form the reconstruction procedure (on an elemental level) can be written in the form

$$\mathbf{u_i} = \mathbf{g_{ij}^*}\, \bar{u}_j \qquad \text{for} \quad 1 \leqslant j \leqslant N, \quad 1 \leqslant i \leqslant N, \tag{29}$$

where

$$g_{ij}^* = G_j(x_i). \tag{30}$$

Based on these N point values the interpolating polynomial $u(x)$ can then be constructed from Eq. (26). This local reconstruction procedure is then repeated for all elements. To form a global interpolating polynomial however we need to impose a continuity condition at elemental interfaces as we explain in the next section.

2.3. *Interfacial Constraint*

The interpolation polynomial $u(x)$ constructed based on the Gauss–Lobatto–Chebyshev points is of degree N while the polynomial we obtain from the reconstruction procedure is of degree $(N-1)$. The additional information needed to uniquely define $u(x)$ comes from requiring continuity of the solution at the interfacial nodal points. For the kth element for example we require that its rightmost nodal value and the leftmost nodal value of element $(k+1)$ will be equal (say, to some value u_γ). This can be accomplished for $(k+1)$th element by adding an extra term to the $(N-1)$th order polynomial, as

$$u^{k+1}(r) = \sum_{j=1}^{N} \bar{u}_j^{k+1} G_j(r) + (1-r)\, T'_N(r)\, \frac{\delta u^k}{2N^2}, \tag{31}$$

where δu^k can be defined by

$$\delta u^k = u_\gamma - \sum_{j=1}^{N} \bar{u}_j^{k+1} G_j(-1). \tag{32}$$

Here the coordinate $r \in (-1, 1)$ refers to the local element coordinate (see Section 2.1). Note that the expression $(1-r)\, T'_N(r)$ attains zero values at all the Gauss–Lobatto–Chebyshev points of the $(k+1)$th element except the leftmost one. Therefore, implementing (31), (32) is equivalent in practice to requiring only the leftmost point value to be equal to u_γ. The rest of the point values of the $(k+1)$th element remain unchanged. The same will be true for the kth element and its rightmost point value. The only undetermined quantity is u_γ. The value of u_γ should be set either to $\sum_{j=1}^{N} \bar{u}_j^{k+1} G_j(-1)$ or to $\sum_{j=1}^{N} \bar{u}_j^k G_j(1)$, depending on the direction (i.e., sign of the advection velocity) of the problem. We will elaborate on this point in Section 4.

3. CELL AVERAGES AND RECONSTRUCTION: DISCONTINUOUS FUNCTION

The main difficulty in applying spectral methods to approximating discontinuous solutions is the Gibbs phenomenon. If a discontinuous function is approximated by a spectral expansion (Chebyshev, Fourier, etc.), the approximation is only $O(1/N)$ accurate in smooth regions and contains $O(1)$ oscillations near the discontinuity. When spectral methods are applied to partial differential

equations with discontinuous solutions, the Gibbs phenomenon may also lead to numerical instability.

An interesting approach to construct a non-oscillatory spectral approximation to a discontinuous function has been recently proposed in [2]. Let $u(x)$ be a piecewise C^∞ function with a jump discontinuity at point x_s and with a jump $[u]_{x_s}$. The key idea in [2] was to augment the Fourier spectral space with a sawtooth function. It was shown that the approximation using the augmented spectral space will be non-oscillatory if the sawtooth function approximates the magnitude and the location of the discontinuity with *second-order* accuracy. The discontinuity parameters can be determined with specified accuracy based on the spectral expansion coefficients. More recently, it was pointed in [4] that a first-order accurate approximation of discontinuity magnitude also leads to non-oscillatory behavior.

In this work we extend this approach and apply it in the context of the spectral element methodology. Let us denote for simplicity the entire array of cell averages defined at the Gauss–Chebyshev points (see Fig. 3) (regardless of which element they belong to) by $\bar{u}_J$

$$\bar{u}_J \qquad \text{for} \quad 1 \leqslant J \leqslant KN,$$

where K is the number of spectral elements covering the domain and N is the number of Gauss–Chebyshev points in each element. We also denote by u_I the entire array of point values defined at the Gauss–Lobatto–Chebyshev points (as shown in Fig. 3), i.e.,

$$u_I \qquad \text{for} \quad 0 \leqslant I \leqslant KN.$$

3.1. *Reconstruction of Point Values*

We assume that the cell-averaged values of a discontinuous function $\bar{u}_J$ are given. Here we propose a new non-oscillatory reconstruction algorithm based on a simple and reliable procedure for estimating the discontinuity parameters with specified accuracy and incorporating this information in the numerical process. The main steps of the algorithm are as follows:

ALGORITHM R

- Step 1. Find a cell J_s such that

$$|\bar{u}_{J_s+1} - \bar{u}_{J_s-1}| = \max_{2 \leqslant J \leqslant KN-1} |\bar{u}_{J+1} - \bar{u}_{J-1}|.$$

- Step 2. Determine the discontinuous component,

$$\bar{u}_J^d = \begin{cases} \bar{u}_{J_s-1}, & \text{if} \quad 1 \leqslant J \leqslant J_s - 1 \\ \bar{u}_{J_s}, & \text{if} \quad J = J_s \\ \bar{u}_{J_s+1}, & \text{if} \quad J_s + 1 \leqslant J \leqslant KN. \end{cases}$$

- Step 3. Determine the continuous component,

$$\bar{u}_J^c = \bar{u}_J - \bar{u}_J^d \qquad \text{for} \quad 1 \leqslant J \leqslant KN.$$

- Step 4. Find I_s^-, I_s^+ such that J_s denotes the cell corresponding to the interval $[x_{I_s^-}, x_{I_s^+}]$ (thus define the reconstructed values of the discontinuous part of the solution),

$$u_I^d = \begin{cases} \bar{u}_{J_s-1}, & \text{if} \quad 0 \leqslant I \leqslant I_s^- \\ \bar{u}_{J_s+1}, & \text{if} \quad I_s^+ \leqslant I \leqslant KN. \end{cases}$$

- Step 5. Obtain point values u_I^c from $\bar{u}_J^c$ using the procedure presented in Section 2 (Eq. (26)).
- Step 6. Obtain

$$u_I = u_I^c + u_I^d \qquad \text{for} \quad 0 \leqslant I \leqslant KN.$$

It is obvious that the pair of cell averages $\bar{u}_{J_s-1}$ and $\bar{u}_{J_s+1}$ represents the discontinuity magnitude with first-order accuracy. It has been shown in [10] (and it also follows from the more general argument presented in [17]), however, that three cell averaged values $\bar{u}_{J_s-1}$, $\bar{u}_{J_s}$, and $\bar{u}_{J_s+1}$ contain information about the discontinuity location up to second-order accuracy. However, our algorithm does not require explicit information about the discontinuity location. As a result, we obtain a very simple and reliable algorithm for non-oscillatory reconstruction. The current algorithm is based entirely on the cell averaged values in the physical space and not on the coefficients of a spectral expansion. Therefore, it fits naturally into the context of the spectral element method.

3.2. *Cell Averages*

As in the smooth case we assume that the point values of a function are known and that the function contains a single jump discontinuity at the point x_s. Again, we decompose a given discrete function into two parts: discontinuous and smooth. The smooth part can be averaged using the procedure described in Section 2; the cell averages corresponding to the discontinuous part can be computed directly using the following algorithm:

ALGORITHM A.

- Step 1. Find point values I_s^+, I_s^- such that

$$x_{I_s^-} \leqslant x_s \leqslant x_{I_s^+}.$$

- Step 2. Evaluate the discontinuous component

$$u_I^d = \begin{cases} u_{I_s^-}, & \text{if} \quad 0 \leqslant I \leqslant I_s^- \\ u_{I_s^+}, & \text{if} \quad I_s^+ \leqslant I \leqslant KN. \end{cases}$$

- Step 3. Obtain the continuous component

$$u_I^c = u_I - u_I^d \quad \text{for} \quad 0 \leqslant I \leqslant KN.$$

- Step 4. For the cell corresponding to the interval $[x_{I_s^-}, x_{I_s^+}]$, defined by J_s, determine

$$\bar{u}_J^d = \begin{cases} u_{I_s^-}, & \text{if} \quad 1 \leqslant J < J_s \\ \dfrac{u_{I_s^-}(x_s - x_{I_s^-}) + u_{I_s^+}(x_{I_s^+} - x_s)}{x_{I_s^+} - x_{I_s^-}}, & \text{if} \quad J = J_s \\ u_{I_s^+}, & \text{if} \quad J_s < J \leqslant KN. \end{cases}$$

- Step 5. Evaluate $\bar{u}_J^c$ for $1 \leqslant J \leqslant KN$ applying the averaging procedure to u_I^c $(0 \leqslant I \leqslant KN)$ according to (18).
- Step 6. Define $\bar{u}_J = \bar{u}_J^c + \bar{u}_J^d$ for $1 \leqslant J \leqslant KN$.

4. HYPERBOLIC EQUATIONS

We use three standard examples in order to present numerical experiments with the aforementioned algorithm: the linear advection problem and the inviscid Burgers equation and then one-dimensional Euler equations of gas dynamics.

4.1. *Linear Advection*

The model problem we consider is the initial value problem given by

$$\begin{aligned} &u_t + a u_x = 0, \\ &u(x, 0) = \phi(x), \\ &u(0, t) = \psi(t), \end{aligned} \tag{33}$$

where $\phi(x)$ and $\psi(t)$ are given functions and a is a constant representing the advection velocity. The interfacial condition is imposed according to the sign (direction) of the advection speed as

$$u_\gamma = \begin{cases} u_0^{k+1}, & \text{if} \quad a < 0, \\ u_N^k, & \text{if} \quad a \geqslant 0. \end{cases} \tag{34}$$

4.2. *Inviscid Burgers Equation*

The model problem we consider is the initial value problem for the inviscid Burgers equation,

$$\begin{aligned} &u_t + \left(\frac{u^2}{2}\right)_x = 0, \\ &u(x, 0) = \phi(x), \\ &u(0, t) = \psi(t). \end{aligned} \tag{35}$$

Note, that the Burgers equation can be rewritten in quasi-linear form as

$$u_t + u u_x = 0. \tag{36}$$

It is clear from (36) that u plays the role of the advection velocity in this case. To impose the interfacial continuity constraint we determine the direction according to the Roe-speed (see [15])

$$\tilde{a} = \frac{u_N^k + u_0^{k+1}}{2}, \tag{37}$$

and thus

$$u_\gamma = \begin{cases} u_0^{k+1}, & \text{if} \quad \tilde{a} < 0, \\ u_N^k, & \text{if} \quad \tilde{a} \geqslant 0. \end{cases} \tag{38}$$

4.3. *One-Dimensional Euler Equations of Gas Dynamics*

The system of Euler equations for polytropic gas in one dimension is given by:

$$\mathbf{u}_t + \mathbf{f}(\mathbf{u})_x = 0, \tag{39}$$

with

$$\mathbf{u} = \begin{pmatrix} \rho \\ m \\ E \end{pmatrix}, \qquad \mathbf{f} = \begin{pmatrix} \rho q \\ qm + P \\ q(P + E) \end{pmatrix}, \tag{40}$$

$$P = (\gamma - 1)(E - \tfrac{1}{2}\rho q^2), \tag{41}$$

where ρ denotes density, q is velocity, P pressure, E total energy, $m = \rho q$ is the momentum, and γ is the ratio of the specific heats of a polytropic gas. While the discretization of the Euler system using the cell-averaging approach is straightforward, the imposition of the interfacial condition requires further discussion.

Interfacial Condition. Consider the Jacobian matrix of the system given by $A(\mathbf{u}) = \partial \mathbf{f}/\partial \mathbf{u}$. The right-eigenvectors of A are

$$\mathbf{r}_1(\mathbf{u}) = \begin{pmatrix} 1 \\ q - c \\ H - qc \end{pmatrix}, \qquad \mathbf{r}_2(\mathbf{u}) = \begin{pmatrix} 1 \\ q \\ \frac{1}{2}q^2 \end{pmatrix},$$

$$\mathbf{r}_3(\mathbf{u}) = \begin{pmatrix} 1 \\ q + c \\ H + qc \end{pmatrix}, \tag{42}$$

where $c=\sqrt{\gamma P/\rho}$ is the speed of sound and the enthalpy H is defined by

$$H=\frac{(E+P)}{\rho}=\frac{c^2}{\gamma-1}+\frac{1}{2}q^2. \tag{43}$$

The left-eigenvectors of A are

$$\begin{aligned} l_1(\mathbf{u})&=\frac{1}{2c^2}\left((2c+q(\gamma-1))\frac{q}{2},\ -c-q(\gamma-1),\ \gamma-1\right),\\ l_2(\mathbf{u})&=\frac{1}{c^2}\left(c^2-(\gamma-1)\frac{q^2}{2},\ (\gamma-1)q,\ -(\gamma-1)\right),\\ l_3(\mathbf{u})&=\frac{1}{2c^2}\left(-(2c-q(\gamma-1))\frac{q}{2},\ c-q(\gamma-1),\ \gamma-1\right). \end{aligned} \tag{44}$$

Let us denote the matrix of right-eigenvectors of the Jacobian $A=A(\tilde{\mathbf{u}})$ as

$$R=(\mathbf{r}_1(\tilde{\mathbf{u}}),\ \mathbf{r}_2(\tilde{\mathbf{u}}),\ \mathbf{r}_3(\tilde{\mathbf{u}})) \tag{45}$$

and the matrix of left eigenvectors as

$$L=\begin{pmatrix} l_1(\tilde{\mathbf{u}}) \\ l_2(\tilde{\mathbf{u}}) \\ l_3(\tilde{\mathbf{u}}) \end{pmatrix}, \tag{46}$$

where $\tilde{\mathbf{u}}$ is Roe-averaged state between the states $\mathbf{u}_N^k$ and $\mathbf{u}_0^{k+1}$ (see [15]). Then

$$L\cdot A\cdot R=\begin{pmatrix} \lambda_1 & 0 & 0 \\ 0 & \lambda_2 & 0 \\ 0 & 0 & \lambda_3 \end{pmatrix}, \tag{47}$$

where the eigenvalues of A are given by

$$\lambda_1=q-c, \qquad \lambda_2=q, \qquad \lambda_3=q+c. \tag{48}$$

The characteristic variables $\mathbf{v}=L\cdot\mathbf{u}$ can be introduced for both states as

$$\begin{aligned} \mathbf{v}_0^{k+1}&=L\cdot\mathbf{u}_0^{k+1}\\ \mathbf{v}_N^{k}&=L\cdot\mathbf{u}_N^{k}. \end{aligned} \tag{49}$$

Then the values to be imposed at the interface can be defined by

$$(\mathbf{v}_\gamma)_i=\begin{cases} (\mathbf{v}_0^{k+1})_i, & \text{if } \lambda_i<0,\\ (\mathbf{v}_N^{k})_i, & \text{if } \lambda_i\geqslant 0, \end{cases} \qquad i=1,2,3, \tag{50}$$

and can be transformed back to the physical variables by

$$\mathbf{u}_\gamma=R\cdot\mathbf{v}_\gamma. \tag{51}$$

A similar procedure can be used to impose Dirichlet boundary conditions.

5. ALGORITHM

The main steps of the proposed spectral element non-oscillatory algorithm are as follows:

- Step 1. Employ Algorithm A to evaluate field of cell averages $\bar{u}_J(0)$ on the Gauss–Chebyshev mesh corresponding to the initial condition $u(x,0)$. (Apply filtering to the smooth component if necessary.)
- Step 2. Compute the transportive fluxes f_I at each Gauss–Lobatto–Chebyshev point. (Apply flux limiters if necessary.)
- Step 3. Advance (explicitly) the cell averages from the previous time level n to obtain $\bar{u}_J^{n+1}$.
- Step 4. Reconstruct point values u_I from the cell averages employing Algorithm R. (Apply filtering to the smooth component if necessary.)
- Step 5. If the target time is not achieved go to Step 2.

In this section we describe in some detail the time-stepping procedure, filtering, and flux-limiting which are used in the overall algorithm.

5.1. *Time Discretization*

An explicit time-stepping scheme is used which corresponds to the Adams–Bashforth scheme of order $M=1$ (Euler), order $M=2$ or 3 in the form

$$\bar{u}_J^{n+1}=\bar{u}_J^{n}-\frac{\Delta t}{\Delta x_J}\sum_{q=0}^{M}\beta_q\,[f_{I^+}-f_{I^-}]^{n-q}, \tag{52}$$

where β_q are appropriate weight coefficients [6]. The higher-order fluxes f_I are computed at the Gauss–Lobatto–Chebyshev points after point values have been reconstructed from the cell averaged field $\bar{u}_J$.

5.2. *Filter*

In our experiments we used the filter developed recently by Vandeven [20]. It is given by

$$\sigma_p(x)=1-\frac{(2p-1)!}{(p-1)!^2}\int_0^x [t(1-t)]^{p-1}\,dt, \tag{53}$$

where p is the order of the filter. This filter is very similar to the raised cosine and sharpened raised cosine for $p=3$ and

$p=8$, respectively (see [5] for the description of these classical filters). It has been shown in [20] that pth-order accuracy can be recovered away from discontinuities.

5.3. *Flux Limiter*

Here we describe a flux limiter used in our experiments. Let us denote by

$$\delta^L = u_I - \bar{u}_{J-1}$$
$$\delta^R = u_I - \bar{u}_J$$

and

$$a_0 = \bar{u}_J - \bar{u}_{J-1}$$
$$a_{-1} = \bar{u}_{J-1} - \bar{u}_{J-2}$$
$$a_1 = \bar{u}_{J+1} - \bar{u}_J.$$

Then we define

$$\Psi_1^L = \max\left(0, \min\left(1, \frac{a_0}{\delta^L}\right)\right),$$
$$\Psi_2^L = \max\left(0, \min\left(1, \frac{a_{-1}}{\delta^L}\right)\right), \tag{54}$$
$$\Psi^L = \min(\Psi_1^L, \Psi_2^L)$$

and evaluate

$$u_I^L = \bar{u}_J + \Psi^L \cdot \delta^L. \tag{55}$$

Following a similar procedure we define

$$\Psi_1^R = \max\left(0, \min\left(1, \frac{a_0}{\delta^R}\right)\right),$$
$$\Psi_2^R = \max\left(0, \min\left(1, \frac{a_1}{\delta^R}\right)\right), \tag{56}$$
$$\Psi^R = \min(\Psi_1^R, \Psi_2^R)$$

and evaluate

$$u_I^R = \bar{u}_{J+1} + \Psi^R \cdot \delta^R. \tag{57}$$

Finally, the flux is computed according to

$$f_I = \tfrac{1}{2}[(f(u_I^R) + f(u_I^L)) - |\tilde{a}_I|\,(u_I^R - u_I^L)], \tag{58}$$

where $\tilde{a}_I$ is Roe-averaged state between u_I^R and u_I^L. Note the apparent similarity of this limiter to Roe non-compressive limiter (see [19]).

6. NUMERICAL RESULTS

In this section we will report several numerical experiments with the developed algorithm, including approximation results, linear advection, inviscid Burgers equation, and the 1D Euler system analyzed in Section 4. The time step used in all the experiments with linear advection, the inviscid Burgers equation, and the 1D Euler system was chosen to be sufficiently small so that errors due the spatial discretization are dominant.

6.1. *Non-oscillatory Averaging and Reconstruction*

Our first experiment is a static non-oscillatory averaging followed by reconstruction. Given are the point values of the function

$$u = \frac{4}{1+\cos^2 y} - 3,$$

where

$$y = \begin{cases} \dfrac{\pi}{40}(x-7), & \text{if } 0 \leqslant x \leqslant 5, \\ \dfrac{\pi}{40}(x-9), & \text{if } 5 < x \leqslant 10. \end{cases} \tag{59}$$

This function has a jump discontinuity at $x_s = 5$. First, we evaluate cell averages of a given discrete function using Algorithm A, and then, we reconstruct the point values from the cell averages using Algorithm R. In Fig. 4 we plot on the logarithmic scale the errors corresponding to three different discretizations. In each case the discretization

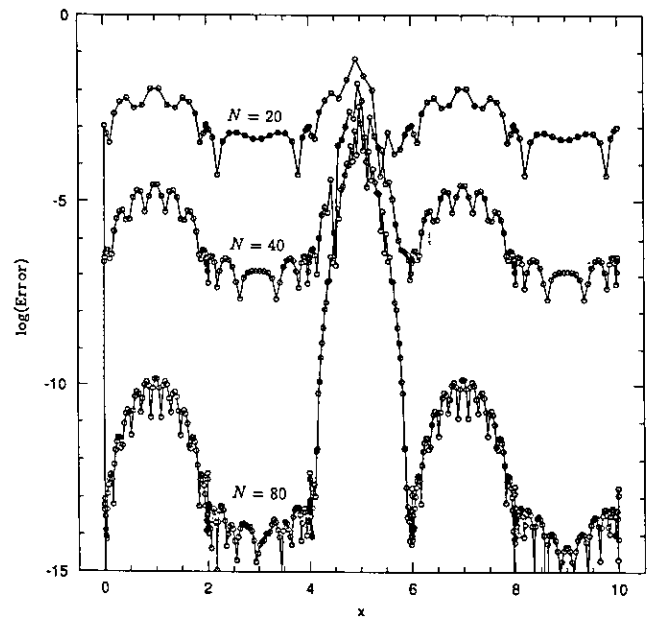

FIG. 4. Averaging and reconstruction of a discontinuous function (see Section 6.1). Pointwise errors on the logarithmic scale, $N = 20$, 40, 80, and $K = 5$.

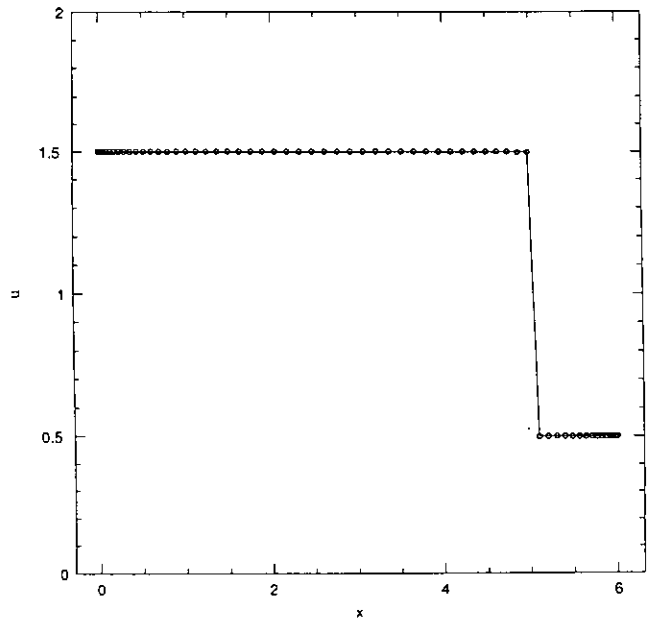

FIG. 5. Linear advection of a discontinuous solution, $N = 64$, $K = 1$ at time $t = 2.0$. (Initial location of discontinuity at $x = 3.0$.)

consists of five spectral elements ($K = 5$), with each element containing $N = 20$, 40, 80 points. The Vandeven filter of orders $p = 5$, 10, 20 was applied for each case, respectively, to the Chebyshev spectrum of the smooth component on each element both in averaging and reconstruction procedure. This filtering was essential in order to obtain an exponential accuracy shown in the Fig. 4 away from discontinuity.

6.2. *Linear Advection of Discontinuous Solution*

Consider the initial boundary value problem for the linear advection problem (33) for $x \in [0, 10]$, $a = 1$, and

$$\phi = \begin{cases} 0.5 & \text{for } x \leqslant 5, \\ 1.5 & \text{for } x > 5. \end{cases}$$

In Fig. 5 we plot the numerical solution for $N = 64$, $K = 1$ (global spectral method) at time $t = 2.0$. Although not to severe this test validates our algorithm of Section 5. In Fig. 6 we plot the numerical solution to problem (33) with initial conditions given by (59) for $N = 40$, $K = 5$ at time $t = 1.0$, and in Fig. 7 we plot the corresponding pointwise error. In this case we see again that spectral convergence is obtained away from the discontinuity. In particular, the upstream part of the solution is resolved spectrally accurate, while errors can propagate downstream in the advection direction and affect the convergence rate. To recover faster convergence everywhere, the errors in the near vicinity of the shock as well as exactly at the shock might be removed using the recently developed one-sided filters (see [3]).

6.3. *Inviscid Burgers Equation*

We consider the initial value problem in the interval $x \in [0, 6]$ with initial conditions given by

$$u(x, 0) = 0.3 + 0.7 \sin \frac{\pi x}{3}.$$

This initially smooth problem develops eventually a shock discontinuity in the solution. The exact solution is easily

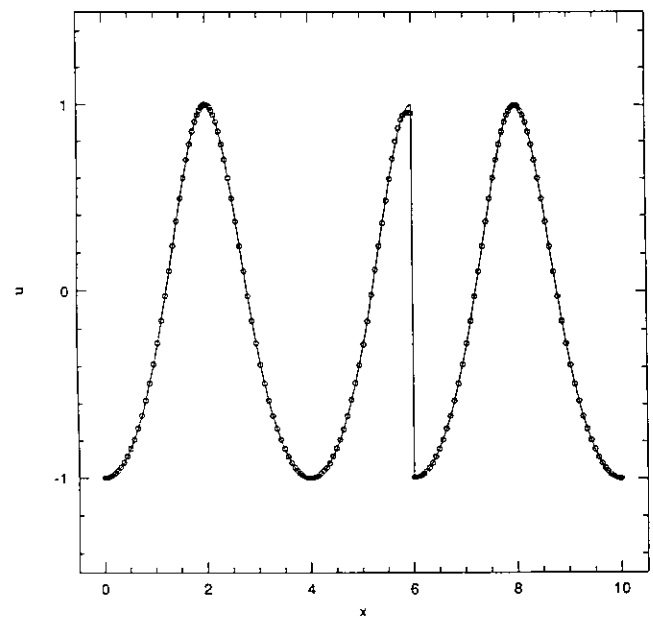

FIG. 6. Linear advection of a discontinuous solution, $N = 40$, $K = 5$ at time $t = 1.0$. (Initial location of discontinuity at $x = 5.0$.)

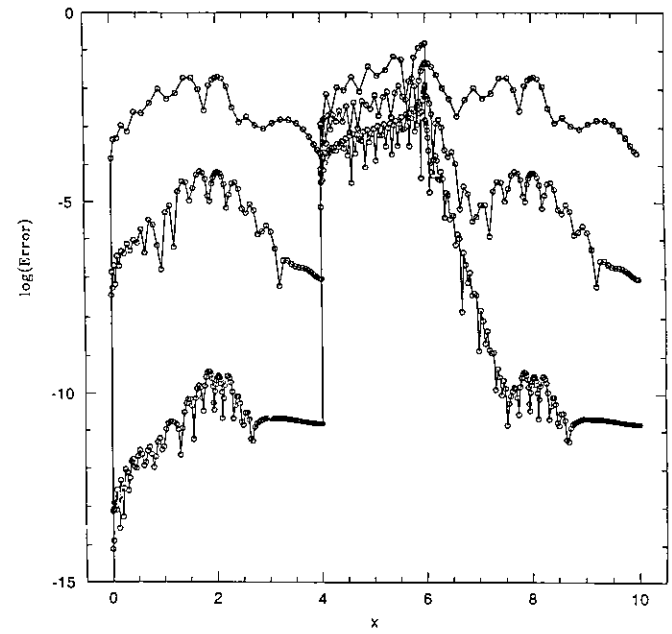

FIG. 7. Pointwise error of the linear advection problem (previous figure) at time $t = 1.0$, $K = 5$, and $N = 20$, 40, and 80.

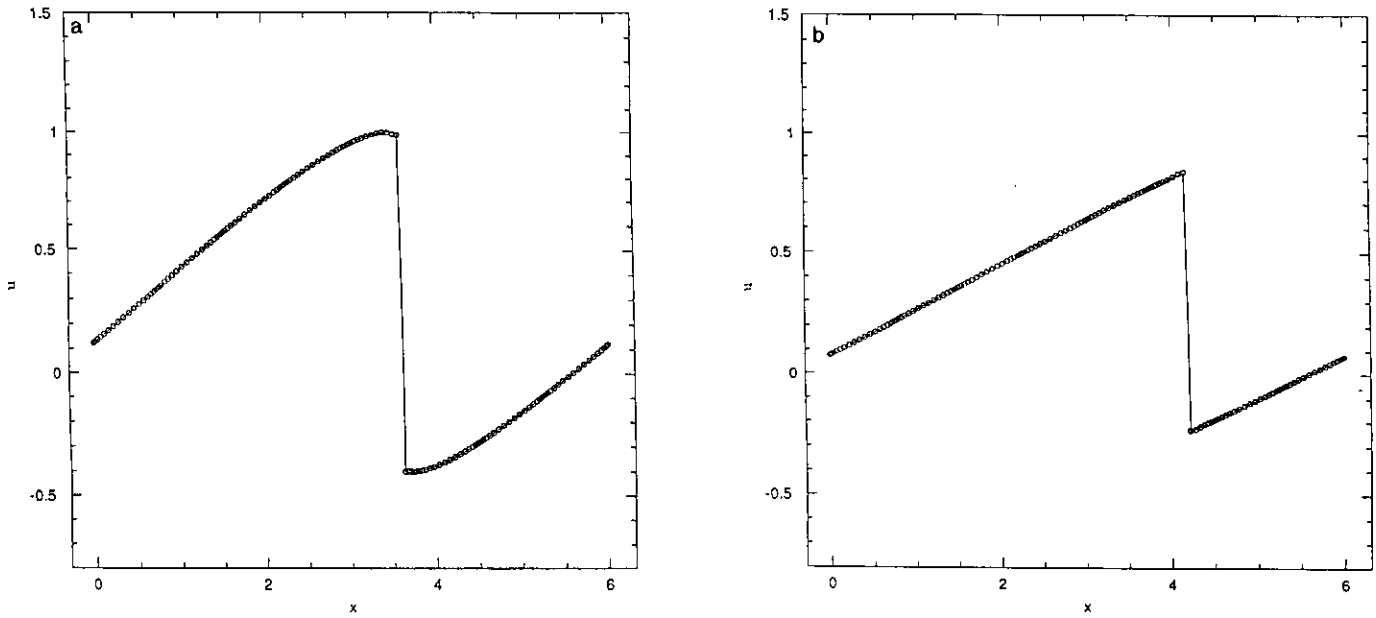

FIG. 8. (a) Solution to inviscid Burgers equation for $N=20$, $K=8$ at time $t=2.0$. Initial conditions given by $u(x,0)=0.3+0.7\sin(\pi x/3)$. (b) Same as the previous figure except time $t=4.0$.

obtained and is used for the testing of the proposed algorithm.

In Fig. 8 we plot the solution for $N=20$, $K=8$ at time $t=2.0$ (a) and $t=4.0$ (b). The pointwise errors are plotted on the logarithmic scale on Fig. 9 for $K=8$ and $N=5$, 10, 20. The Vandeven filter of orders 4, 8, and 16, respectively, was used. In all these experiments the non-oscillatory reconstruction was performed after the estimated discontinuity magnitude became larger than 0.4. (We observed that the results are not very sensitive to the particular value of the threshold.) Also, the limiter described in Section 5.3 was employed here in the interval of 10 gridpoints around the cell containing discontinuity (except at points next to that cell—one on each side). In order to avoid any influence of *non-positive* time stepping (as Adams–Bashforth is) around the shock we used forward Euler time stepping to advance cell averages. We found in our experiments with this example, that applying the *global* Chebyshev spectral method with non-oscillatory reconstruction and filtering the spectrum of the smooth part resulted in a very poor accuracy ($O(1)$ error) in the large part of the domain. This seems to be related to the creation of shock in this case. Large differences occur between several cell averaged values at that time. However, our non-oscillatory reconstruction method treats only three subsequent cells. Applying flux limiters in this part of the domain restores algebraic convergence there. Employing spectral elements leads to localization of this region within one element, as we observe in Fig. 9.

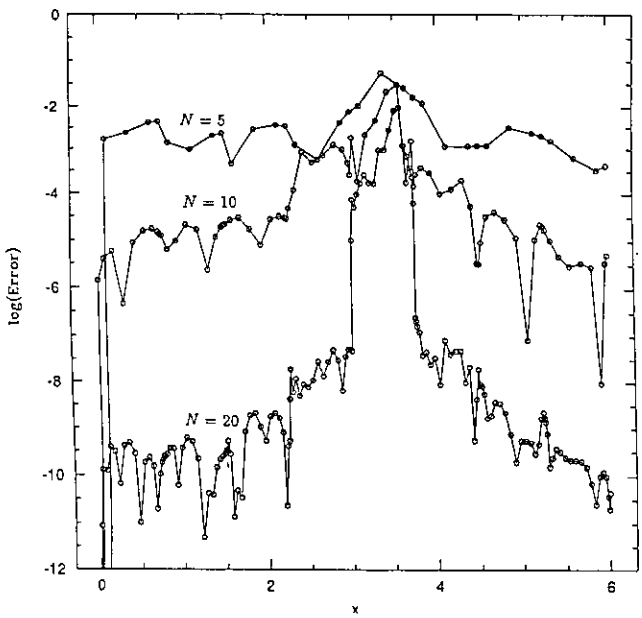

FIG. 9. Errors in the solution of the inviscid Burgers equation. Initial conditions given by $u(x,0)=0.3+0.7\sin(\pi x/3)$. Time $t=2.0$, $N=5$, 10, 20, and $K=8$.

6.4. *One-Dimensional Euler Gas Dynamics Equations*

Here we present our numerical experiments with the test problem considered in [1, 4]. We consider the following initial condition for (39),

$$\begin{aligned} &\rho_l = 3.857143, \quad q_l = 2.629367, \\ &P_l = 10.33333, \quad -5 \leqslant x \leqslant -4, \\ &\rho_r = 1 + \varepsilon \sin \pi x, \quad q_r = 0, \quad P_r = 1, \\ &-4 < x \leqslant 5, \end{aligned} \tag{60}$$

where $\varepsilon = 0.2$. The solution to (60) models the interaction between a moving shock and sinusoidal density disturbances (see [1, 4]). In Fig. 10a we display the density profile for $N = 10$ and $K = 22$ (corresponding to 199 grid points) at time $t = 1.8$. The discontinuity cell was located using the momentum equation. For comparison we also plot the solution obtained by the second-order MUSCL scheme with $N = 200$ in Fig. 10b. Figures 10(c)–(e) present our experiments with the same problem, but with $N = 5$ and $K = 55$ (221 grid points). Observe that the fourth-order approximation is sufficient in this case to capture the essential features of the solution for all the variables

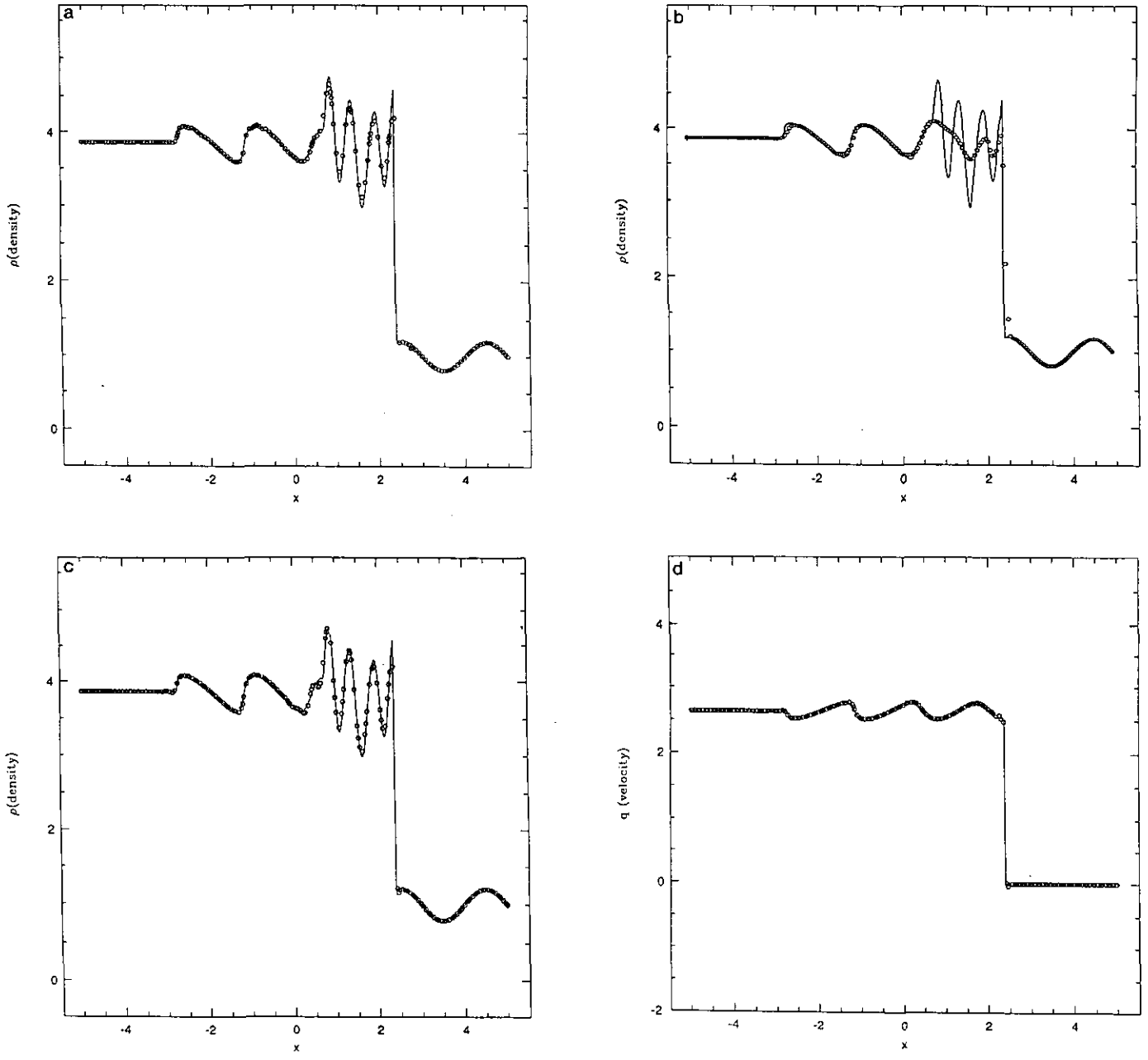

FIG. 10. (a) Interactions between a shock wave and density waves with $N = 10$, $K = 22$ (199 grid points) at time $t = 1.8$. The solid represents the solution obtained by the third-order ENO finite difference method with 1200 grid points (courtesy of Wai-Sun Don and David Gottlieb, Brown University). The circles correspond to our solution. (b) The same problem as in the previous figure. Result obtained by a second-order MUSCL scheme using 200 grid points (courtesy of Wei Cai and Chi-Wang Shu). (c) The same problem as in the previous figure, except for $N = 5$, $K = 55$ (221 grid points). (d) Velocity plot corresponding to the same case as in the previous figure. (e) Pressure plot corresponding to the same case as in the previous figure. (f) The same problem as in the previous figures, except for $N = 20$, $K = 15$ (286 grid points).

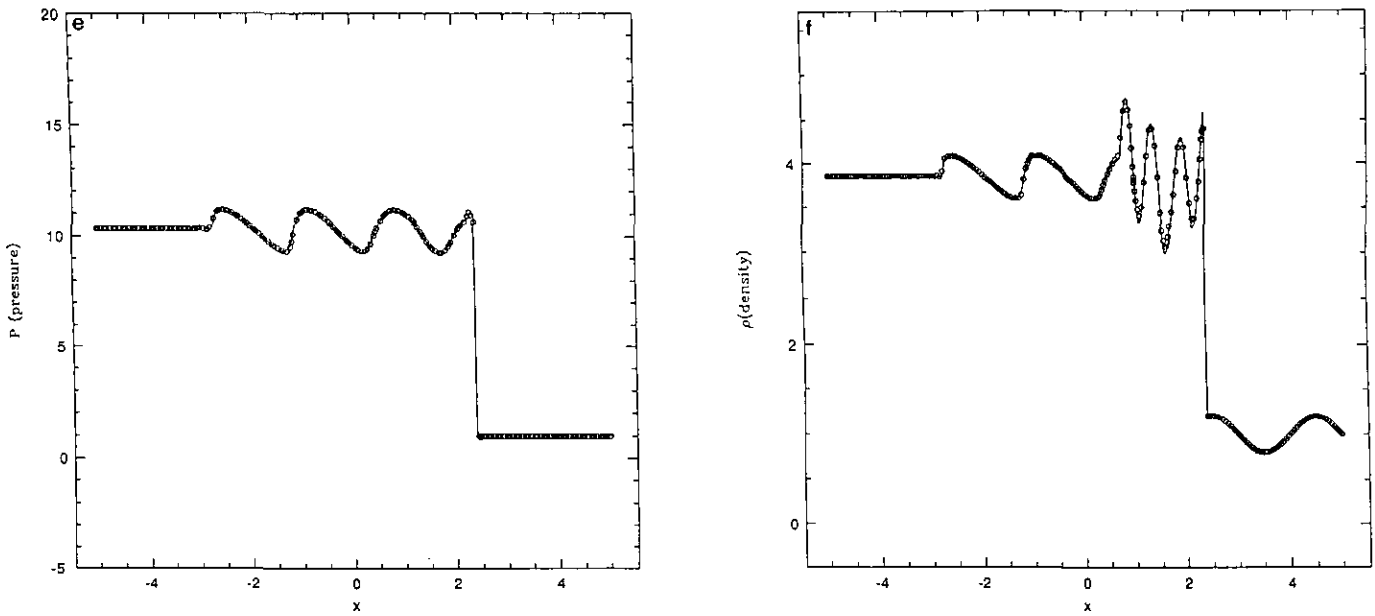

FIG. 10—*Continued*

(density, velocity, and pressure). Fig. 10f corresponds to the experiment with the same problem with $N = 20$ and $K = 15$ (286 grid points).

7. DISCUSSION

In this work we have formulated and tested an algorithm based on spectral element discretization and essentially non-oscillatory approximations concepts. The results show that this approach leads to a stable method, capable of producing very accurate solutions away from discontinuities. The convergence of the method in a small neighborhood around the shock is still of low-order, however recent developments of one-sided filters [3, 18] will allow us to recover accuracy in the shock region too. The multi-domain algorithm we present here can easily accomodate such implementations.

The method is capable of resolving very accurately fine structures arising from interactions of shocks with disturbances (see Fig. 10). Such structures correspond to a wide spectrum of frequencies and are typical in shock wave/boundary layer interactions encountered in simulations of compressible turbulence. The generalization of the present method for the case of multiple discontinuities is straightforward. However, the method in its current form is not capable of treating rarefaction waves due to the artificial compression introduced by the method at discontinuities.

Recent work using spectral element discretizations and flux corrected transport (FCT) limiters [7, 8] shows a clear superiority of high-order methods in resolving shock waves (representing them by transition layers of one to two meshpoints wide) and rarefactions. However, the spectral accuracy of these methods in the smooth regions is questionable. Currently we are working on a hybrid algorithm based on FCT limiters and non-oscillatory approximations, which will allow us to obtain sharp shocks and treat rarefactions properly, while at the same time obtain good accuracy away from discontinuities.

As regards the computational complexity of the method, the cell-averaged formulation is as efficient as the pointwise formulation in one space dimension. In two and three space dimensions, the cell-averaged formulation becomes more costly than the pointwise formulation. However, the cell-averaged formulation may still be desirable in the latter case because of its genuinely multi-dimensional character [8].

ACKNOWLEDGMENTS

We thank Professor David Gottlieb for many helpful suggestions. We also thank John Giannakouros and Anne Bourlioux for many stimulating discussions. This work was supported by AFOSR Grant 90-0261.

REFERENCES

1. W. Cai, D. Gottlieb, and A. Harten, "Cell Averaging Chebyshev Methods for Hyperbolic Problems," in *Comput. Math. Appl.* Advances in PDE (Academic Press, London/New York, 1990).
2. W. Cai, D. Gottlieb, and C. Shu, *Math. Comput.* **52**, 389 (1989).
3. W. Cai, D. Gottlieb, and C. Shu, *SIAM J. Numer. Anal.* **29** (1992).
4. W. Cai and C. Shu, *J. Comput. Phys.*, to appear.
5. C. Canuto, M. Hussaini, A. Quarteroni, and T. Zang, *Spectral Methods in Fluid Dynamics* (Springer-Verlag, New York/Berlin, 1987).

6. C. W. Gear, *Numerical Initial Value Problems in Ordinary Differential Equations* (Prentice-Hall, Englewood Cliffs, NJ, 1973).
7. J. Giannakouros and G. E. Karniadakis, Spectral element-FCT method for scalar hyperbolic conservation laws, *Int. J. Num. Meth. Fluids* **14**, 707 (1992).
8. J. Giannakouros, D. Sidilkover, and G. E. Karniadakis, *Comput. Methods Appl. Mech. Engrg.*, to appear.
9. D. Gottlieb and S. A. Orszag, *Numerical Analysis of Spectral Methods: Theory and Applications* (SIAM, Philadelphia, 1977).
10. A. Harten, *J. Comput. Phys.* **83**, 148 (1989).
11. G. E. Karniadakis, *Appl. Numer. Math.* **6**, 85 (1989).
12. G. E. Karniadakis, E. T. Bullister, and A. T. Patera, "A Spectral Element Method for Solution of Two- and Three-Dimensional Time Dependent Navier–Stokes Equations," in *Finite Element Methods for Nonlinear Problems* (Springer-Verlag, New York/Berlin, 1985), pp. 803.
13. Y. Maday and A. T. Patera, "Spectral Element Methods for the Navier–Stokes Equations," ASME, State-of-the-art surveys in Computational Mechanics, 1989.
14. A. T. Patera, *J. Comput. Phys.* **54**, 468 (1984).
15. P. L. Roe, *J. Comput. Phys.* **43**, 357 (1981).
16. E. M. Rønquist, Ph.D. thesis, Massachusetts Institute of Technology, 1988 (unpublished).
17. D. Sidilkover, High order shock locating methods, submitted for publication.
18. A. Solomonoff and D. Gottlieb, private communication.
19. P. K. Sweby, *SIAM J. Numer. Anal.* **21**, 995 (1984).
20. H. Vandeven, *J. Sci. Comput.* **6**, 159 (1991).